nature photonics

ARTICLES

PUBLISHED ONLINE: 29 JUNE 2014 | DOI: 10.1038/NPHOTON.2014.111

Truncated-correlation photothermal coherence tomography for deep subsurface analysis

Sreekumar Kaiplavil* and Andreas Mandelis*

Photothermal diffusion-wave imaging is a promising technique for the analysis of a range of media. However, traditional diffusion-wave techniques are limited by the physics of parabolic diffusion and can only produce depth-integrated planar images. Here, we report a depth-resolved photothermal imaging modality, henceforth termed truncated-correlation photothermal coherence tomography (TC-PCT). This enables three-dimensional visualization of subsurface features, which is not possible with known optical or photothermal imaging techniques. Examples include imaging of solids with intricate subsurface structures and discontinuities, such as holes in steel, burn depth profiles in tissues, and the structure of bone. It is compatible with regulations concerning maximum permissible exposure and is the photothermal analogue of optical coherence tomography. Axial and lateral resolutions in bone are measured to be ~25 and 100 μm, respectively, with a depth range of ~3.2 mm (approximately four thermal diffusion lengths).

The science of diffusion waves has been the focus of intense interest since the middle of the nineteenth century[1–3]. In the last four decades, in particular, there has been rapid growth in this parabolic-wave-governed energy or matter transport research, which encompasses several subdisciplines, including thermal waves, diffuse photon density waves and excited-carrier plasma waves[4–8]. In contrast to electromagnetic or acoustic waves, which are described in terms of hyperbolic differential equations, diffusion waves lack wavefronts and are reflection- and refraction-less in nature[9]. Detection of distance-integrated, rather than localized, distributions of energy is a unique characteristic of diffusion-wave fields. For parabolic diffusion-wave fields, both stationary and drifting, energy migration across the contributing frequency modes is strongly lossy. So, an energy-preserving completeness relation linking the time-domain propagation of a diffusive energy impulse with a complete stationary frequency spectrum cannot be defined. As a consequence of the loss of frequency modes, non-localization and spreading of diffusive impulses occur at the expense of coherence between time and the depth of energy propagation. This leads to poor axial resolution, which deteriorates with time and distance from the source and is a serious limiting factor of diffusion waves. Historically, the first attempt to localize energy in a thermal-wave field was made by using pseudorandom binary sequence (PRBS) optical excitation followed by cross-correlation signal processing[10]. Later, the frequency-modulated time-delay technique was proven to have a faster response and improved dynamic range compared to the PRBS scheme[11]. Significant progress in this area was made with the attainment of binary-phase-coded thermal coherence tomography[12]. The energy localization achieved with thermal coherence tomography, although incomplete, enables the deconvolution of thermal responses from axially discrete sources and improves the depth resolution in thermal diffusion-wave imaging. All these methods utilize matched filtering using pulse compression, which is a traditional radar technique for enhancing the range resolution and signal-to-noise ratio (SNR)[13] in a hyperbolic wave field. Here, the coded signal can be described by the frequency response $H(\omega)$ of the coding filter. The frequency response of the matched filter that receives the signal is the complex conjugate $H^*(\omega)$ of the coding filter response. The output of the matched filter is the inverse Fourier transform of the product of the signal spectrum and the matched filter response:

$$y(t) = \frac{1}{2\pi}\int_{-\infty}^{\infty} |H(\omega)|^2 e^{i\omega t}\,\mathrm{d}\omega \qquad (1)$$

Compared to harmonic signals, the clear advantage of a short pulse capable of maintaining a flat power spectrum over a very broad bandwidth, even under diffusive attenuation losses, recently inspired us to introduce chirped-pulse thermal-diffusion-wave radar[14]. In this case, the advantages of a highly compressed output with negligible side-lobe power distribution led to a much improved SNR and depth profiling capability. This approach is particularly attractive for the optothermal analysis of biological samples, in which infrared absorption by water molecules and the maximum permissible exposure (MPE) ceiling[15] for the excitation fluence appreciably limit the measurable thermal-diffusion-wave signal. However, in the case of diffusion waves, the limited frequency bandwidth afforded by signal coding cannot encompass widely varying frequency contents as time evolves and spatial coordinates change. This leads to incomplete or limited localization and loss of coherence on timescales and associated spatial locations outside the completeness bandwidth.

Poor efficiency or SNR and the lack of control over axial resolution, which in turn hinders the three-dimensional visualization of subsurface features, are known shortcomings of traditional radar approaches for thermal-diffusion-wave applications to systems with intricate or complex subsurface structures, such as biological specimens. Accordingly, what is required is a method to extend the completeness relation across very wide ranges of diffusion-wave field frequency spectra. In this Article, we introduce a three-dimensional photothermal imaging modality called truncated-correlation photothermal coherence tomography (TC-PCT), which exhibits the highest degree of energy localization in a parabolic diffusion wave field to date through time-evolving filtering controlled by pulse delay and truncation. Although the full thermal-wave frequency spectrum in a given experimental configuration is set

Center for Advanced Diffusion-Wave Technologies, Department of Mechanical and Industrial Engineering, University of Toronto, 5 King's College Road, Toronto, Ontario M5S 3G8, Canada. *e-mail: sreekumarkaiplavil@yahoo.co.in; mandelis@mie.utoronto.ca

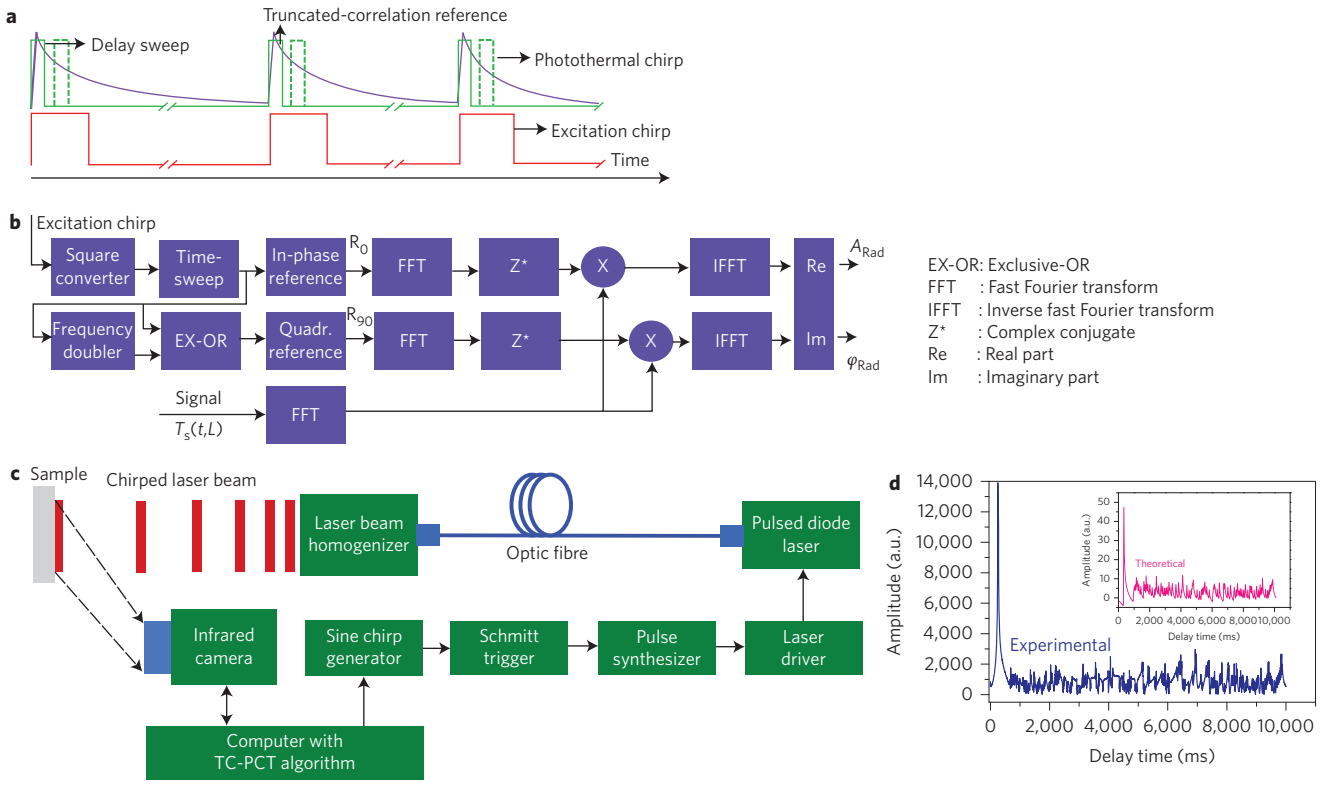

Figure 1 | Principle of TC-PCT. a, The truncated reference chirp, synthesized from the laser excitation chirp, is subjected to a controlled phase increment that determines the penetration depth. The truncated pulse width is much smaller than the repetition period. The shorter the pulse width, the better the axial resolution; however, the minimum is set by the speed of the infrared camera. **b**, The frequency-domain TC-PCT algorithm. The photothermal relaxation chirp is cross-correlated with the truncated-reference chirp in a pixel-by-pixel manner to generate planar images corresponding to the depth set by the reference phase delay. The frequency-domain computation offers faster execution of the algorithm. **c**, Block schematic of the imaging system. **d**, Theoretical and experimental results for the TC-PCT output. The SNR floor ratio (dynamic range) is high (~15) due to the excellent SNR and significant side-lobe suppression capability of the pulsed-chirp radar.

by the excitation optical pulse, the truncated cross-correlation process provides a time-evolving filter that preserves coherence in the part of the frequency spectrum within the instantaneous time window. Therefore, the effect of correlation truncation is to preserve the energy within the instantaneous frequency bandwidth with no or minimal loss, despite the diffusive nature of the signal. Over the entire thermal relaxation process, the cumulative effects of energy preservation within the wide spectral bandwidth spanned sequentially through the time-evolving filter make the parabolic diffusive response spectrum resemble the spectral characteristics of a propagating lossless hyperbolic wave field. Also, its response resembles the cross-correlation and pulse compression image processing familiar from radar science. In conclusion, time-evolving filtering through cross-correlation truncation results in pulse-compression-linewidth-limited depth-resolved images with axial and lateral resolution well beyond the well-known thermal-diffusion-length-limited, depth-integrated nature of conventional thermographic modalities[16–18]. As a consequence, a highly axially resolved layer-by-layer ('sharp' or 'crisp') photothermal image sequence can be obtained, capable of reconstructing three-dimensional visualizations (tomograms) of photothermal features in wide classes of materials. As a further consequence of its depth-resolved nature, TC-PCT also exhibits subsurface depth profiling/imaging capabilities well beyond those of conventional thermal-wave modalities[4,5] (by a factor of ~4).

Physics of TC-PCT

Two of the major outcomes of the propagating wave description of diffusion-wave fields are the existence of a complex wavenumber and the dispersive characteristics stemming from the fact that the phase velocity is frequency dependent. In terms of the transport parameter (diffusivity α for thermal waves) and angular frequency ω, the effective phase velocity is defined as $v = \sqrt{2\alpha\omega}$, allowing faster diffusive wave propagation at higher frequencies, which is also true for hyperbolic waves. The frequency spectrum of a thermal relaxation signal following a short-pulsed excitation is continuous. The surface temperature relaxation amplitude is therefore scaled in terms of depth below the surface, such that the early transient strength corresponds to shallow regions while late portions correspond to deeper zones. The truncated chirped pulse can be synthesized from the optical excitation chirp as shown in Fig. 1a (not drawn to the actual timescale). For optical chirp generation we used a pulsed semiconductor laser, the current feed line of which has a finite inductance. At higher currents (a few tenths of an ampere or more) the back e.m.f. across the feed line introduces a significant rise and fall time that is not negligible compared to the pulse width. The shorter the truncated pulse duration, the greater the axial resolution will be due to the improvement in energy localization. Obviously, this implies that if the truncated pulse chirp is replaced by an expanded pulse chirp so that the pulse duration becomes comparable with the thermal relaxation time, then a depth-integrated, rather than depth-resolved, thermal-wave picture of the sample will emerge through the radar channels. In this limit, TC-PCT would assume the features of regular lock-in thermography[16,19]. Irrespective of pulse width, the delay-sweep increment determines the depth sampling interval. The truncated-correlation radar cross-correlates the thermal relaxation chirp with a split/sliced reference chirped pulse whose width

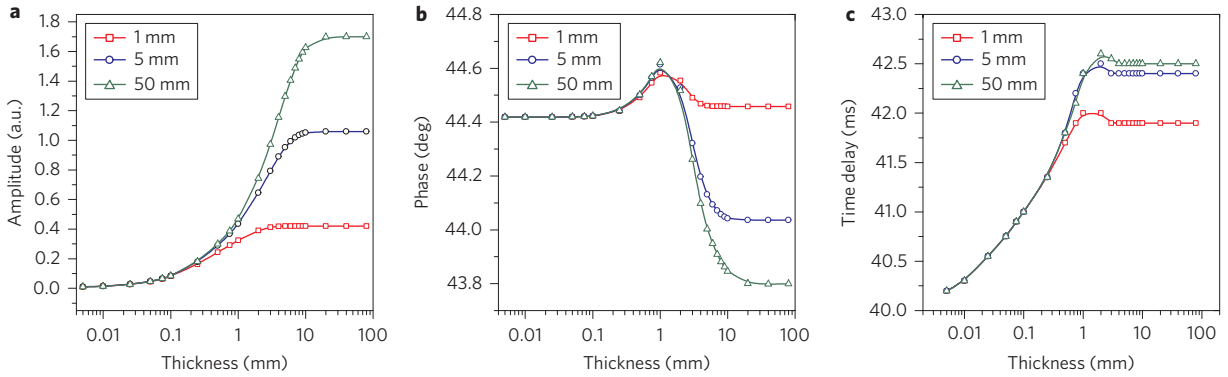

Figure 2 | Simulation results. The dependence of the truncated-correlation radar output parameters on the absorber depth below the sample surface for optical absorption lengths ($l_a = 1/\mu_a$) of 1, 5 and 50 mm has been studied theoretically. l_a = 1–5 mm is the typical range of absorption depth in cortical bones (goat) at 808 nm. Bone diffusivity is taken as 5×10^{-7} m^2 s^{-1}. A 0.1–0.5 Hz, 25 s chirp with a pulse width of ~5 ms was used for the simulation. **a**, Variation of amplitude. The one-to-one correspondence between the amplitude and absorber depth up to about four diffusion lengths is an unprecedented attainment, as the traditional photothermal amplitude depth range is limited to approximately one diffusion length. **b**, Variation of initial phase. Here also, the signal is sensitive to absorber depth up to about four diffusion lengths. **c**, Variation of peak time delay. Although depth-sensitive, the range is shorter than the other two parameters.

is shorter than the excitation pulse width (Fig. 1a). This truncated correlation leads to an ultra-narrow pulse compression linewidth, such that the falling edge of the compressed pulse (Fig. 1d) carries a highly depth-resolved signature of the photothermal features of the sample, the depth being coded in terms of delay time. By incrementing the initial phase/delay of the truncated-reference chirp and sampling the radar output at a fixed position, one can obtain a sequence of time-coded data that yields a depth-coded photothermal profile of the medium. Using an infrared camera, the evolution of sample surface temperature can be recorded and the output can be translated to a sequence of frames of two-dimensional depth-coded images with a high degree of localization. These images can be stacked to produce a volume visualization of the photothermal properties of the sample. This truncated-reference swept-correlation process in the time domain is analogous to a continuously tunable bandpass filter in the frequency domain. While the operating/central frequency is controlled by the delay of the trimmed chirped pulse with respect to the excitation pulse, the pass-bandwidth or quality factor is determined by the truncated-pulse width. In truncated cross-correlation thermal-diffusion-wave fields, the delay controls the depth while the truncated-pulse width determines the degree of energy localization or axial resolution. Theoretical expressions for the thermal-wave radar amplitude (A_{Rad}) and phase (φ_{Rad}) are developed in Supplementary Section A in terms of the in-phase/quadrature output of the chirped-pulse photothermal radar, $Rad_{0/90}$.

The energy localization of this thermal-wave modality offers unprecedented axial resolution[10–12] throughout the diffusive relaxation process and is thus capable of subsurface imaging of systems with intricate structures (see also section 'Axial and lateral resolution of TC-PCT'). One of our key interests is the three-dimensional visualization of bones, especially the trabecular structure through cortical and soft tissue overlayers, for the purpose of early diagnosis of osteoporosis[20]. Figure 2 shows the theoretical dependence of amplitude, delay time and initial phase (phase for which delay is zero) channels on the depth of signal-generating absorbers below the sample surface. For simulation, a diffusivity of 5×10^{-7} m^2 s^{-1} and a range of absorption coefficients (at 808 nm) of 0.2–1.0 mm^{-1} are considered, which are typical of human bones. A third value of 0.02 mm^{-1} was also used as an extreme case of optical transparency in tissues. The starting and ending chirp frequencies were 0.1 and 0.5 Hz, respectively. The chirp period was 25 s and the half power pulse width was ~5 ms, the reciprocals of these durations being the lower and upper frequency limits of the chirp power spectrum. Under these conditions the thermal diffusion length ($l_d = \sqrt{2\alpha/\omega}$) in bone assumes a maximum and minimum of ~1.9 mm and 28 μm, respectively. As μ_a increases, the source of thermal-wave generation approaches the surface and consequently the thermal centroid moves closer to the plane of detection, because the peak delay time, which is related to $\tau_t = 1/\alpha\mu_a$, an optothermal time constant indicating heat conduction from a depth equal to the optical penetration length, is anticorrelated with the optical absorption coefficient. For depths smaller than the longest diffusion length (1.9 mm), the delay time for a given absorption coefficient increases with sample thickness or with the position of the thermal-wave centroid within the sample. This is the region in which thermal-wave interference exists due to confinement within the sample. As the thickness approaches the diffusion length, interference effects produce a maximum and the delay remains saturated for depths greater than ~3.5 mm, effectively indicating a semi-infinite configuration. This means that the delay channel theoretically carries depth information up to a thickness of about two diffusion lengths. The initial phase becomes a minimum around the longest diffusion length, as interference effects tend to disappear and contributions to the thermal centroid from the back-surface interactions (accumulation or depletion) become negligible. Thereafter, the delay keeps on increasing with thickness. For optical absorption length l_a = 1 mm, when the thickness is greater than the thermal diffusion length, the sample is thermally and optically thick and the phase tends to saturate at a depth of ~($l_d + l_a$). If $L > l_a > l_d$, then phase saturation occurs around 8 mm ($4l_d$) and is independent of l_a, in agreement with the known photothermal response of optically and thermally thick solids[21]. This means that within four thermal diffusion lengths, TC-PCT phase imaging can reveal significant subsurface information, well beyond the range (~1.5 diffusion lengths) of conventional photothermal phase imaging techniques. The lack of uniqueness in the vicinity of $L = l_d$ is not a generic feature and its extent is parameter dependent. The peak-amplitude channel approaches a saturation value around a depth of ~($l_d + l_a$) if l_a = 1 mm. For $l_a > l_d$, like the initial phase, the amplitude channel carries depth information up to about four diffusion lengths. The amplitude decreases with a decrease in l_a as the thermal gradient is higher for shorter depths. In this case, the rate of energy transfer by diffusion into the colder bulk (heat sinking) of the sample is higher than that for extended heating (higher values of l_a). The amplitude channel has

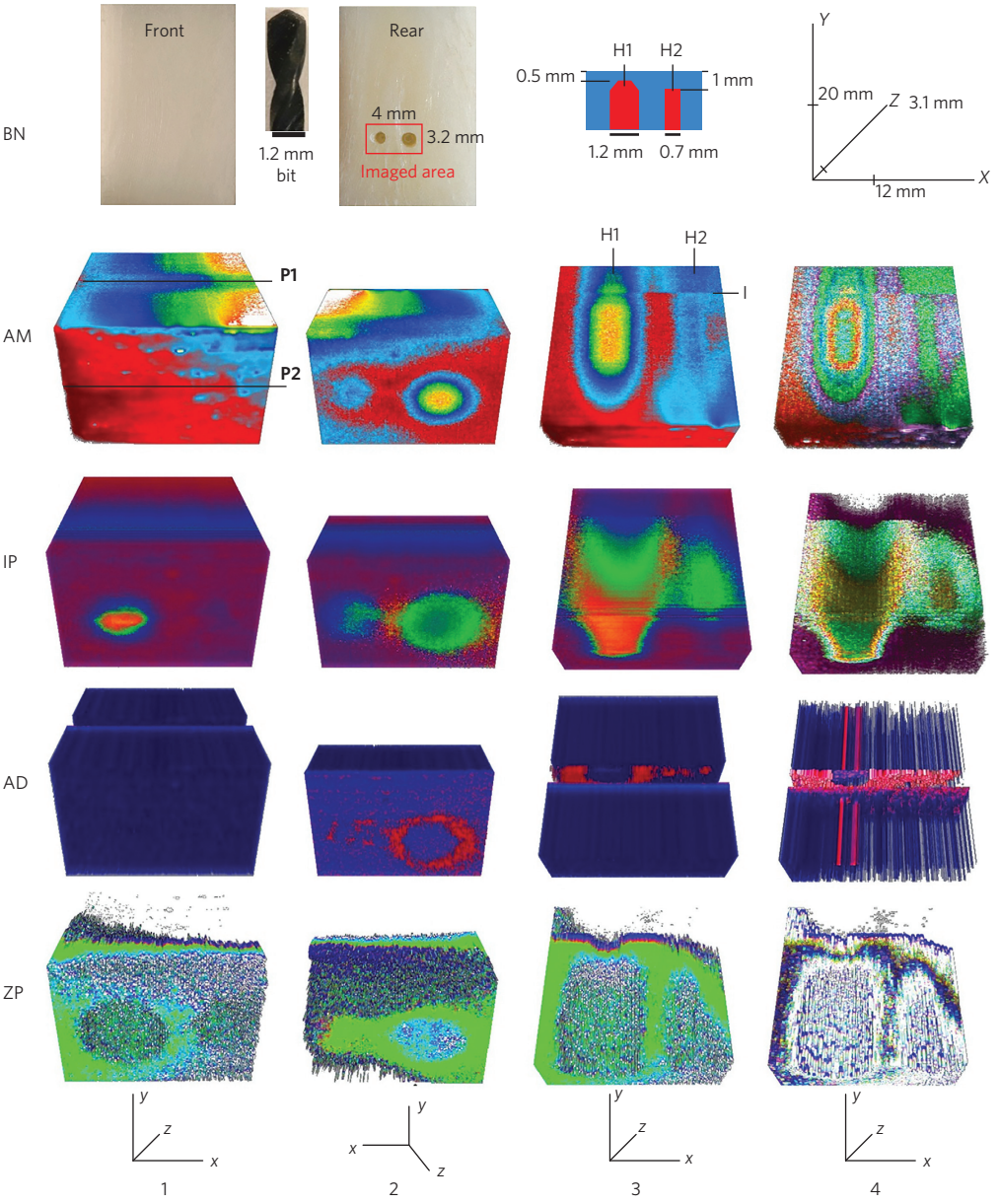

Figure 3 | Proof of concept. A 4-mm-thick cortical bone slab extracted from a goat femur, with two holes, was used to generate various TC-PCT images to validate the theory. A 0.2–0.6 Hz, 12 s chirp of 10 ms pulse width and 40 W peak power was used for excitation. The truncated reference pulse width was 2 ms, leading to an axial resolution of ~25 μm in bone. BN1–4, goat bone sample, geometry of holes and coordinate system for BN1. The coordinate systems for various angles of view (see text for details) are shown at the bottom. AM1–4, TC-PCT amplitude tomogram. The energy accumulation at the rear bone–air boundary is observable in the *x*–*z* plane around layer I in AM3. IP1–4, initial phase tomogram. Like the amplitude, this channel maintains a depth range of about four diffusion lengths. AD1–4, amplitude-delay tomogram. Compared to amplitude and phase, the depth range is limited for the delay. ZP1–4, zero-crossing phase-delay tomogram. This channel monitors the dynamic steady state in a layer-by-layer manner when there is no net thermal-wave propagation across it. Despite limited energy localization capacity, this channel too can monitor the subsurface conditions.

the key advantage of high dynamic range and sensitivity based on a one-to-one correspondence with the thickness, thus paving the way for a unique depth reconstruction over about four diffusion lengths. This is the maximum depth ever attained in the evolution of thermal-diffusion-wave physics[4,5,12,16].

Proof of concept

TC-PCT was implemented in a LabView environment with a frequency-domain cross-correlation algorithm for faster execution and is shown in Fig. 1b along with the outline of the TC-PCT imaging system (Fig. 1c). Instrumentation and signal generation details are provided in the Methods. Truncated correlation tomograms of a goat femur were recorded (Fig. 3) to investigate the proof of principle and limitations of TC-PCT as a tomographic imaging modality (see Methods). The results showed that initial-phase tomograms exhibit a limited dynamic range, particularly for shallow regions, which in turn leads to depth-overlapping near the front surface. The high temporal uncertainty (~2.7 ms) of our infrared camera limits the axial resolution of the time-delay (amplitude-delay) channel. In any case, the depth range is limited to about one diffusion length. In conclusion, based on the results of Fig. 3, the rest of this Article focuses on TC-PCT amplitude because of its superior performance in terms of sensitivity and unique depth-resolving capability compared to the other channels.

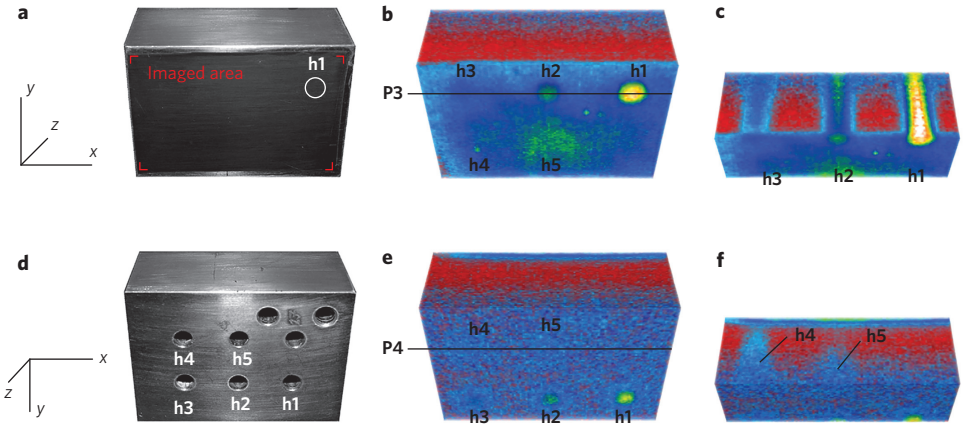

Figure 4 | Opaque material tomography. The capability of TC-PCT for three-dimensional imaging of internal defects in opaque materials, a case of broad interest in the non-destructive evaluation of engineering materials, has been tested. **a**, Irradiated surface of a steel block with its coordinate system. The surface coating (~10 μm thick) enhances the SNR for the available laser peak power (~40 W). At elevated laser power or energy (shorter wavelengths) this absorber layer can be avoided. **b**, Amplitude tomogram as observed from the blackened surface. **c**, Cross-sectional view obtained by numerically slicing **b** in the *x*–*z* plane at P3. **d**, Rear view of the block with coordinates rotated by 180°. **e**, Amplitude tomogram as observed from the rear surface. **f**, Cross-sectional view obtained by slicing **e** in the *x*–*z* plane at P4. Holes h1 and h2 are clearly visible through the black layer because the higher thermal diffusivity of steel (compared to bone) makes the diffusion time of flight across the steel overlayer above h1 and h2 shorter than the temporal resolution of the camera. Improved axial resolution necessitates the use of faster cameras in high-diffusivity materials.

Axial and lateral resolution of TC-PCT

The axial resolution of TC-PCT is controlled chiefly by the width of the truncated-reference pulse and sample thermal diffusivity. Therefore, the resolution is material dependent and increases as the truncated-reference pulse width decreases. However, there is a limit imposed by the speed of the infrared camera on the shortest possible pulse width. For our camera, the temporal resolution was ~2.7 ms. We fixed the minimum truncated-reference pulse width to 2 ms. To evaluate the axial resolution in bone, the truncated pulsed chirp radar waveform ('chirp-1') was considered. A mechanically polished, ~100-μm-thick, cortical bone slab (30×10 mm^2) extracted from the goat femur already mentioned was used as the sample. An absorbing mark was drawn on the back surface using graphite, and the sample was wetted to prevent direct radiative coupling of infrared photons. TC-PCT was performed by irradiating (808 nm) the front surface with several truncated-reference pulse widths: 2, 4, 6, 8, 10 and 12 ms. Given that bones are highly heterogeneous in their physical properties, TC-PCT was obtained at different locations. On average, the back absorber mark appeared in the TC-PCT image for widths greater than 8 ms. For a 200-μm-thick bone slab this occurred at a pulse width of ~16 ms. Extrapolating this response, a bone axial resolution of ~25 μm for a 2 ms reference was estimated. In comparison, in steel the resolution was found to be ~700 μm, a consequence of its higher diffusivity (see next section for details). Higher axial resolution is achievable using faster cameras, permitting the use of more narrowly truncated references.

A visual inspection was carried out to assess the lateral resolution. For this we examined the binarized amplitude TC-PCT of an intact goat rib (Supplementary Fig. 1). The amplitude data were binarized such that those above and below a threshold could be designated as Boolean '1' and '0', respectively, to depict the physical presence or absence of thermal-wave power at a point within the sample. The binarized three-dimensional data were subjected to surface-mesh formation to visualize the volume distribution with adjustable transparency. This binarized amplitude tomogram is independent of the absolute photothermal amplitude and has advantages in the structural examination of bones. This will be reported in a subsequent publication, which will expand on the foundational ideas presented here. It is evident that trabecular structures laterally thinner than 100 μm have been resolved. For a given material, imaging area and chirp parameters, the lateral resolution is controlled by the camera resolution, which, for our camera, is 320×256 pixels. Yet another performance figure is the speed of operation or analysis time. This is mainly controlled by the chirp period. The use of longer chirps improves the extent of energy localization[13] and the depth range, although it slows down the imaging procedure, both data capture and reconstruction. The imaging field (area) can be arbitrarily increased provided the camera resolution is sufficiently high to maintain good TC-PCT image quality. The performance figures of comparable imaging modalities will be discussed in the following sections in the context of the several case-study applications.

TC-PCT imaging of opaque materials

The ability of TC-PCT to interrogate the subsurface features of strongly surface-absorbing samples such as metals has been verified by considering the response of a surface-blackened steel block ($6.0 \times 4.5 \times 3.0$ cm^3) with multiple holes (0.5 cm diameter) drilled from the bottom to align axially along the direction of one-dimensional thermal-wave propagation (Fig. 4a). Holes h1–h5, which are resolved in the amplitude tomograms with chirp-1 waveform excitation and 2 ms truncated reference, have steel overlayer thicknesses of ~0.27, 0.45, 0.62, 1.18 and 1.68 mm from the top, respectively. The amplitude tomogram is sliced along P3 in the *x*–*z* plane of Fig. 4b for viewing holes h1–h3 (Fig. 4c). Holes h1 and h2 are clearly visible through the black layer as a consequence of the higher (compared to bone) thermal diffusivity of steel, which makes the diffusion time of flight across the steel overlayer above h1 and h2 shorter than the temporal resolution of the camera. The tomogram is further sliced at P4 in the *x*–*z* plane (Fig. 4e) to expose holes h4 and h5 (Fig. 4f). In support of the abovementioned time-of-flight hypothesis, h4 and h5 are axially resolved, even though progressive significant signal attenuation has decreased the depth-profiling image contrast SNR. In general, higher-diffusivity materials would need an appropriately higher-speed infrared camera for improved axial resolution in this tomographic approach. SNR, and hence depth range, can be increased by using a higher laser peak power and/or a more sensitive camera. Employing longer chirps is yet another solution.

Table 1 | Quantitative comparison of properties of three non-ionizing, non-invasive techniques for bone diagnostics.

Technique	Depth range (mm)	Lateral resolution (μm)	Axial resolution (μm)	Signal-to-baseline ratio (dynamic range)	Demineralization sensitivity	Typical speed to analyse 1.0 × 1.0 × 0.1 cm^3 at the specified resolution (s)	Reference
Photoacoustics (3 MHz)*	~3	~1,000	~1,000	4–6	High (cortical) Low (trabecular)	>10	Current studies
Photoacoustics (20 MHz)*	~1.3	~500	~100	4–6	Unknown	>40	Current studies
OCT	≤1	10–15 (in practice)	~5 (or better)	~2	Moderate	<1	Refs S31–S33; technical specifications: Zeiss Cirrus-5000
TC-PCT	~3.2 mm (or better)	100 (or better)	25 (or better)	~15	High (cortical) High (trabecular)	~12	Current studies and ref. 14

*No rigorous investigations have yet been carried out in this direction. The quantities presented here are estimates from a few preliminary trials.

Detailed studies of the first TC-PCT applications for the functional and structural evaluation and early mineral loss monitoring in bones will be presented in a future publication. Although this is the first report of the general concept and principle of TC-PCT, a rigorous investigation of the potential of TC-PCT for bone demineralization tracking has been carried out, and the results, with micro-computed tomography validation, have been presented in another publication[22]. In view of the very significant application potential of this tomographic imaging modality to osteoporosis diagnosis, and to further explore the possibilities of bulk and surface imaging of absorbing and light-scattering samples through TC-PCT, it is worth comparing it with other non-ionizing bone tomographic modalities while emphasizing the high MPE compatibility advantage of the pulsed chirped radar[14]. Accordingly, other non-ionizing bone tomographies are reviewed in Supplementary Sections B and C, and TC-PCT comparisons with other diagnostic imaging modalities are presented in Supplementary Section D. In Table 1, a quantitative comparison of the salient features of photoacoustics, optical coherence tomography (OCT) and TC-PCT is presented.

TC-PCT in burn depth assessment

Three-dimensional imaging of soft tissues, which is of broad biomedical interest, is yet another area where TC-PCT can deliver sharp images of the topography and crisp photothermal features of distributed optical absorbers. Burn-depth estimation is a typical example where a quick, non-invasive and non-contacting assessment of the depth of a wound is a priority for efficient healing[23–26]. A brief review of burn assessment technologies is provided in Supplementary Section E.

It is well known that heat treatment considerably alters the optical and thermal properties of tissues[27]. Depth-resolved imaging of the spatial distribution of burn-induced variations in the optothermal properties of skin and tissues, fast diagnosis (<1 min, typically), the advantage of excitation-synchronized detection (which greatly suppresses asynchronous signal contributions from the changes in the physiological states of the patient), and so on, are attractive features of TC-PCT as a potential burn diagnosis technology. The usefulness of this tomographic modality for burn-depth assessment has been evaluated using a pig ear sample (~3.0 × 3.0 × 0.8 cm^3). By using a copper strip (~2 × 2 mm^2 contact area) maintained at ~150 °C through resistive heating, two burns were created on the surface (Fig. 5a). Heating duration was 5 s for burn W1 and 10 s for burn W2. The imaged area was ~20 × 16 mm^2. Amplitude tomograms were generated with chirp-1 waveform excitation (Fig. 5b–d). Burn injuries extending down to a depth of ~2.5 mm are observable. W2 is a severe burn, deeper and broader, compared to W1. The extent of alteration of tissue parameters for W2 is higher than that for W1. In the pseudo-colour coding (Fig. 5d), red represents higher amplitudes than yellow. One can also observe yellow traces at the periphery of the TC-PCT map corresponding to W2. This happens because, for W2, the injury is less intense at the outer regions compared to the central portion. In general, milder tissue damage appears in yellow and red/pink corresponds to regions of severe injury. It has been verified that TC-PCT resolves tissue damage much deeper than what could be observed in the pure optical image shown in Fig. 5e. A higher-resolution tomogram was recorded for another burn (W3) on a different pig ear sample (Fig. 5f–j). W3 was made with a 2 × 1 mm^2 hot tip (at 150 °C) by making contact for 3 s. An area of 4.0 × 3.2 mm^2 was imaged. It is noticeable that the superficial-dermal/deep-dermal burn appears slightly broadened compared to the surface picture in the TC-PCT image (Fig. 5h).

Conclusions

TC-PCT has been introduced as the highest-energy localization modality in a parabolic diffusion-wave field to date. TC-PCT uses a pulse-chirped radar approach in which a broadband thermal relaxation chirp is cross-correlated with a sequence of delay-swept and pulse-width-truncated references. The truncated pulse width determines the depth (axial) resolution, while the delay with respect to the excitation chirp controls the depth range. Both parameters are operator selectable. It was found that among the available outputs (amplitude, initial phase, peak delay time and zero-phase delay), the amplitude channel offers the highest dynamic range and sensitivity, capable of depth profiling and thermal-wave reconstruction over approximately four thermal diffusion lengths. This feature has been verified both theoretically and experimentally. By stacking depth-scaled planar images generated through phase incrementing the truncated reference, TC-PCT can create three-dimensional visualizations of the distribution of optothermal parameters of the target similar to optical coherence tomography but with considerably higher depth range (millimetres instead of micrometres). The image sequence can also be binarized to generate a volume visualization that is independent of the absolute photothermal amplitude. Its transparency is adjustable to allow viewing of the interior. As first applications, we have examined examples in the non-destructive evaluation (NDE) of industrial materials and in non-invasive biomedical imaging. These include the imaging of solids with intricate substructures, specifically subsurface holes in steel, trabecular bone structure through cortical and soft tissue overlayers, structural changes in animal bones following artificial osteoporosis (demineralization bone loss) and burn-depth profiles in tissues. Axial and lateral resolutions in bone imaging for the current instrumental configuration are ~25 and 100 μm, respectively, with a depth range of ~3.2 mm. TC-PCT exhibits

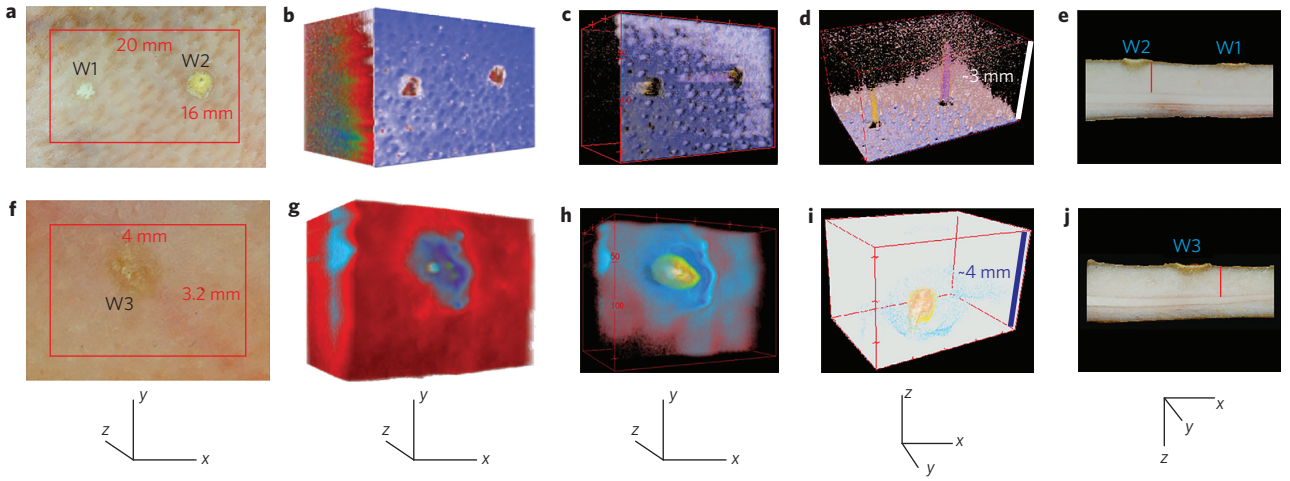

Figure 5 | Application of TC-PCT to burn-depth analysis. In all images, the *z*-axis (depth) is not shown on the actual scale, but has been expanded for clarity. **a**, Photograph of a pig's ear specimen with two burns. The red outline defines the imaged area. **b**, Amplitude tomogram as observed from the tissue surface. **c**, Amplitude tomogram with 60% transparency. The three-dimensional spatial distribution of burn injuries within the tissue can be observed. **d**, Amplitude tomogram with transparency and threshold optimized for burn depth profile inspection. The needle-like structures at the bottom (*x*–*y*) are due to the follicles without hair whose presence can be seen in **a**. **e**, Photograph of the burn cross-section. Red scale bar, ~5 mm. **f**, Photograph of the second sample with burn W3. **g**, Amplitude tomogram as observed from the tissue surface. **h**, Amplitude tomogram with 60% transparency. **i**, Amplitude tomogram with transparency and threshold optimized for burn inspection. **j**, Photograph of the burn cross-section. Red scale bar, ~4 mm.

high sensitivity to cortical bone density, which is very promising for near-surface bone (wrist, tibia, calcaneus and similar) osteoporosis clinical imaging, as there is no need for light penetration into the deeper trabecular region.

Methods

Instrumentation and signal generation. A mid-infrared camera (Cedip 520M, 3.6–5.1 μm spectral response) was used to capture the evolution of sample surface temperature following optical excitation. The linear frequency modulation chirp was generated using a sine chirp synthesizer (Agilent 33220A), the output of which was converted to a corresponding square chirp using a TTL Schmitt trigger circuit. A delay/pulse generator (Stanford Research DG535) converted this square chirp to a pulse chirp, the pulse width being adjustable. This pulse chirp controlled the diode laser (808 nm, 40 W) and was recorded using a high-speed data acquisition module (NI PCI-5122) for synthesizing the truncated reference chirp. The camera frames were stored with its data acquisition provision. The recorded excitation chirp was first converted to a square-wave chirp and then passed through the delay-sweep module. The delay-incremented square-wave chirp ($C_{1f,0}$) was then frequency-doubled ($C_{2f,0}$). Subsequently, $C_{1f,0}$ and $C_{2f,0}$ were subjected to the binary exclusive-OR (EX-OR)[28] operation to generate a quadrature square chirp $C_{1f,90}$. Truncated references R_0 and R_{90} were synthesized from $C_{1f,0}$ and $C_{1f,90}$, respectively. Figure 1d shows theoretical and experimental results for the highly compressed and side-lobe minimized truncated correlation amplitude for a 4-mm-thick cortical bone slab extracted from a goat femur[29]. Its measured μ_a was ~0.33 mm^{-1} at 808 nm and was obtained using the Beer–Lambert law and a variable-thickness bone wedge. Although the Beer–Lambert law does not give accurate results for a scattering sample, the rough estimate obtained for μ_a was sufficient to test the theory.

The experimental truncated pulsed chirp radar parameters, designated a 'chirp-1' waveform, were starting frequency = 0.2 Hz, ending frequency = 0.6 Hz, chirp period = 12 s, excitation pulse width = 10 ms, truncated pulse width = 2 ms and laser peak power = 40 W. The energy per chirp was ~1.92 J and the exposure energy density was ~0.5 J cm^{-2}, well below the MPE ceiling for bone at 808 nm (refs 14,15). The depth-localized profile was timescaled along the falling edge of the compressed pulse. For the truncated correlation tomograms a polished cortical bone slab was extracted from the aforementioned goat femur (Fig. 3), with sample dimensions of 12.0, 20.0 and 3.1 mm along the *x*, *y* and *z* axes, respectively (BN1–4). Two holes with 1.2 mm (H1) and 0.7 mm (H2) diameters were drilled from the rear side such that the bone layer thickness above the holes was ~0.5 and 1.0 mm for H1 and H2, respectively. Two red nylon wire sleeves were inserted tightly into these holes to ensure localized optical absorption. The imaged area was 4.0 × 3.2 mm^2 on the front (*x*,*y*) surface. The camera was operated at 370 frames s^{-1}. A chirp-1 waveform with a sweep-delay step of 2 ms was used to generate a stack of 150 two-dimensional pseudo-colour images, allowing a 300 ms sweep duration. A three-dimensional image (tomogram) was composed by stacking these planar pictures using ImageJ software[30]. All tomograms in column-1 were vertically sliced at P1 across the top *x*–*y* plane, and the half volume was rotated by 180° to generate the images in column-2, depicting the corresponding interior cross-sections. The image volume in column-1 was further sliced horizontally at P2 on the *x*–*z* plane to generate column-3, which shows the depth-resolving capability of this imaging modality. Column-4 is the edge-detected[31] version of column-3, which enhances the boundaries and provides better sensitivity to the geometry of optothermal inhomogeneities. H1 was made with a sharp-tipped regular drill bit and H2 with a flat-tip grinding bit. The bit-tip feature is clearly revealed in the depth-resolved reconstruction in AM3, the top feature of H1. H2 is somewhat obscured by a strongly absorbing inhomogeneity near the top-right corner, which is a characteristic feature of most biological specimens. In any case, the capability of this modality to resolve subsurface features hidden below this photothermally active overlayer is further demonstrated in row AM in Fig. 3. The energy accumulation at the rear bone–air boundary is observable in the *x*–*z* plane around layer I. In general, this energy accumulation is a manifestation of the thermal-wave impedance mismatch at the rear boundary and is characterized by the relative thermophysical properties of the sample and backing material. The resolution of the initial-phase tomogram (IP1–4) is deteriorated by the non-unique response around a depth equal to the diffusion length, as well as by the limited dynamic range, particularly for shallow regions, which in turn lead to depth-overlapping near the front surface. However, this is not a generic feature and its strength is parameter dependent. Hence, this signal channel would be useful to probe deeper regions, of about four diffusion lengths, as the phase variation with depth is within an experimentally resolvable band. The time-delay (amplitude-delay) tomogram (AD1–4) carries depth information for a thin segment. In any case, the depth range is limited to about one diffusion length. Here, zero-phase delay (yet another channel) refers to a dynamic steady state for the corresponding layer across which there is no net thermal-wave propagation. Because material other than the layer of interest is not in a thermal steady state at any time, this channel leads to quasi-static thermal volume imaging. Despite the limited axial resolution, this dynamic steady-state energy distribution is sensitive to subsurface features (ZP1–4).

Image processing. The TC-PCT algorithm in the LabView environment generates sequentially named depth-coded planar (.jpeg) images. All further processing is carried out using ImageJ. A suitable number of planar images are stacked and subjected to three-dimensional visualization with adjustable transparency and orientation for absolute parameter tomography. For binarized amplitude tomography, the stack of planar amplitude images is first binarized using the Huang algorithm available in the 'stack to binary' plug-in. The binarized three-dimensional data are subjected to a surface-mesh formation process to reconstruct the binarized amplitude TC-PCT.

Photography. All photographs were captured using a 24 megapixel digital single-lens reflex camera with a 30 mm, F/2.8 lens.

Safety. All experiments, including sample preparation, were carried out in accordance with the bio- and laser-safety regulations of the University of Toronto.

Received 10 October 2013; accepted 17 April 2014; published online 29 June 2014

References

1. Bell, A. G. On the production and reproduction of sound by light. *Am. J. Sci.* **20,** 305–324 (1880).
2. Bell, A. G. Upon the production of sound by radiant energy. *Phil. Mag.* **11,** 510–528 (1881).
3. Lord Rayleigh. The photophone. *Nature* **23,** 274–275 (1881).
4. Rosencwaig, A. *Photoacoustics and Photoacoustic Spectroscopy* (Wiley, 1980).
5. Almond, D. P. & Patel, P. M. *Photothermal Science and Techniques* (Chapman & Hall, 1996).
6. Mandelis, A. Diffusion waves and their uses. *Phys. Today* **53,** 29–34 (2000).
7. Mandelis, A. *Diffusion-Wave Fields* (Springer, 2001).
8. Bialkowski, S. E. *Photothermal Spectroscopy Methods for Chemical Analysis* (Wiley-Interscience, 1995).
9. Mandelis, A., Nicolaides, L. & Chen, Y. Structure and the reflectionless/refractionless nature of parabolic diffusion-wave fields. *Phys. Rev. Lett.* **87,** 020801 (2001).
10. Kirkbright, G. F. & Miller, R. M. Cross-correlation techniques for signal recovery in thermal wave imaging. *Anal. Chem.* **55,** 502–506 (1983).
11. Mandelis, A. Frequency modulated (FM) time delay photoacoustic and photothermal wave spectroscopies. Technique, instrumentation, and detection. Part I: Theoretical. *Rev. Sci. Instrum.* **57,** 617–621 (1986).
12. Tabatabaei, N. & Mandelis, A. Thermal coherence tomography using match filter binary phase coded diffusion waves. *Phys. Rev. Lett.* **107,** 165901 (2011).
13. Levanon, N. & Mozeson, E. *Radar Signals* (Wiley, 2004).
14. Kaiplavil, S. & Mandelis, A. Highly depth-resolved chirped pulse photothermal radar for bone diagnostics. *Rev. Sci. Instrum.* **82,** 074906 (2011).
15. American National Standard for Safe Use of Lasers, ANSI Z136.1 (Laser Institute of America, 2007).
16. Breitenstein, O. & Langenkamp, M. *Lock-In Thermography: Basics and Use for Functional Diagnostics of Electronic Components* (Springer-Verlag, 2003).
17. Gaiduk, A., Yorulmaz, M., Ruijgrok, P. V. & Orrit, M. Room-temperature detection of a single molecule's absorption by photothermal contrast. *Science* **330,** 353–356 (2010).
18. Tabatabaei, N., Mandelis, A. & Amaechi, B. T. Thermophotonic radar imaging: an emissivity-normalized modality with advantages over phase lock-in thermography. *Appl. Phys. Lett.* **98,** 163706 (2011).
19. Vollmer, M. & Möllmann, K.-P. *Infrared Thermal Imaging* (Wiley-VCH, 2010).
20. White, T. D. & Folkens, P. A. *The Human Bone Manual* (Elsevier Academic, 2005).
21. Rosencwaig, A. & Gersho, A. Theory of the photoacoustic effect with solids. *J. Appl. Phys.* **47,** 64–69 (1976).
22. Kaiplavil, S., Mandelis, A. & Amaechi, B. T. Truncated-correlation photothermal coherence tomography of artificially demineralized animal bones: two- and three-dimensional markers for mineral loss monitoring. *J. Biomed. Opt.* **19,** 026015 (2014).
23. Herndon, D. N. *Total Burn Care* (Elsevier, 2007).
24. Monstrey, S., Hoeksema, H., Verbelen, J., Pirayesh, A. & Blondeel, P. Assessment of burn depth and burn wound healing potential. *Burns* **34,** 761–769 (2008).
25. Jaskille, A. D., Shupp, J. W., Jordan, M. H. & Jeng, J. C. Critical review of burn depth assessment techniques: Part I. Historical review. *J. Burn Care Res.* **30,** 937–947 (2009).
26. Jaskille, A. D., Shupp, J. W., Jordan, M. H. & Jeng, J. C. Critical review of burn depth assessment techniques: Part II. Review of laser Doppler technology. *J. Burn Care Res.* **31,** 151–157 (2010).
27. Welch, A. J. & van Gemert, M. J. C. (eds) *Optical-Thermal Response of Laser-Irradiated Tissue* (Plenum, 1995).
28. Malvino, A. P. & Leach, D. P. *Digital Principles and Applications* (McGraw-Hill, 1994).
29. Romer, A. S. & Parsons, T. S. *The Vertebrate Body* (Saunders College, 1986).
30. ImageJ. See http://rsb.info.nih.gov/ij/
31. Plataniotis, K. N. & Venetsanopoulos, A. N. *Color Image Processing and Applications* Ch. 4 (Springer-Verlag, 2000).

Acknowledgements

A.M. acknowledges a Fellowship award from the Canada Council Killam Research Fellowships Program, which made this research possible. A.M. and S.K. further acknowledge the support of the Ontario Ministry of Research and Innovation (MRI) for the 2007 (inaugural) Discovery Award in Science and Engineering to A.M.; the Canada Research Chairs Programs; the Federal and Provincial Governments for a CFI-ORF award; and the Natural Sciences and Engineering Research Council of Canada for a Discovery and a Strategic Grant. The authors thank Xueding Wang, Department of Radiology, University of Michigan, for recording the PAM of a few rib bone samples.

Author contributions

S.K. conceived the idea, formulated the theory and conducted simulations, developed one pulsed laser unit and a few pulse processing circuits, assembled/developed the instrumental hardware and Labview programs for chirp generation, automation and tomography, prepared the bone and soft tissue samples, carried out the experiments and interpreted results. A.M. provided the imaging instrumentation framework, conceived the idea of thermal coherence tomography and pulsed chirped photothermal radar, co-developed with S.K. the concept of the pulsed chirp photothermal radar (precursors of TC-PCT) and provided overall supervision. S.K. wrote the paper, with assistive revisions and inputs from A.M.

Additional information

Supplementary information is available in the online version of the paper. Reprints and permissions information is available online at www.nature.com/reprints. Correspondence and requests for materials should be addressed to S.K. and A.M.

Competing financial interests

The authors declare no competing financial interests.

nature photonics

SUPPLEMENTARY INFORMATION

DOI: 10.1038/NPHOTON.2014.111

SUPPLEMENTARY TOPICS

A. Signal Generation Theory of Truncated-Correlation Photothermal Coherence Tomography

In contrast to time-domain thermal relaxation signals that lack phase, the TC-PCT output gives rise to amplitude, time-delay and phase for the matched filter, all of which can carry depth resolved energy localisation information with more or less sensitivity and dynamic range. Based on the hyperbolic wave description of diffusion waves, a theoretical formalism can be established to discuss the features of these distinct/independent channels in TC-PCT. We consider a homogeneous sample of thickness L in which thermal diffusion waves propagate without "reflection" (accumulation or depletion) except at the irradiated surface-air boundary. Any energy accumulation/depletion at the rear surface is ignored in this theory. This corresponds to the simplest case in which the back surfaces are deep enough so as not to significantly affect the characteristics of TC-PCT. Assuming bulk optical absorption, for one-dimensional heat diffusion the spectral element of the surface temperature of the sample following optical excitation can be expressed in the frequency domain as:

$$\hat{T}_S(\omega,t,L)=\frac{[1-R]I\mu_a\gamma\eta}{4K\sigma(\omega)}\int_0^L e^{i\omega t}e^{-[\mu_a+\sigma(\omega)]x}dx=\frac{[1-R]I\mu_a\gamma\eta}{4K}\left\{\frac{1-e^{-L[\mu_a+\sigma(\omega)]}}{\sigma(\omega)[\mu_a+\sigma(\omega)]}\right\}e^{i\omega t} \quad (1)$$

Here, R is the surface reflectivity at the excitation wavelength, I is the optical intensity, K is the thermal conductivity, μ_a is the optical absorption coefficient, γ is the thermal-wave transmission coefficient at the irradiated surface-air interface and η is the light-to-heat conversion efficiency

DOI: 10.1038/NPHOTON.2014.111

of the sample. σ(ω) is the thermal wavenumber at angular frequency ω. Following pulsed excitation, the resulting transient temperature distribution at the sample surface is spectrally continuous and can be evaluated from the frequency spectrum, equation (1), using the inverse Laplace transform:

$$T_S(t,L)=\frac{[1-R]I\mu_a\gamma\eta}{4K}\frac{1}{2\pi i}\int_{\Gamma-i\infty}^{\Gamma+i\infty}\left\{\frac{1-e^{-L\left[\mu_a+\sigma(s)\right]}}{\sigma(s)\left[\mu_a+\sigma(s)\right]}\right\}e^{st}ds \tag{2}$$

in which, $s=i\omega$. Contour Γ is selected to the left of all poles in the complex plane, so that the system is stable to its right. Equation (2) can be evaluated through Laplace inversion:

$$T_S(t,L)=\frac{[1-R]I\mu_a\gamma\eta\alpha}{4K}e^{t/\tau_t}\left[erfc\left(\sqrt{t/\tau_t}\right)-erfc\left(\frac{L}{2\sqrt{\alpha t}}+\sqrt{t/\tau_t}\right)\right] \tag{3}$$

Here, $\tau_t=1/\alpha\mu_a^{\,2}$ is an optothermal time constant indicating heat conduction from a depth equal to the optical penetration length, and *erfc* refers to the complementary error function. For optical chirp generation we used a pulsed semiconductor laser, so, the optical intensity of the excitation pulse is approximately modeled as a Gaussian temporal profile:

$$I(t)=I_0e^{-\frac{1}{2}\left(\frac{t}{\xi}\right)^2} \tag{4}$$

The pulse duration is adjusted through the Gaussian characteristic time constant ξ. A linear frequency modulated (LFM) pulsed chirp can be synthesized from the corresponding cosine chirp such that a pulse occurs at the zero crossing of every full cycle determined by:

$$\omega_1 t' + k t'^2 = (4n+1)\frac{\pi}{2} \tag{5}$$

Here, ω_1 is the starting angular frequency, *n=0, 1, 2,...* and $k = (\omega_2 - \omega_1)/T$ is the sweep rate. ω_2 and T are the ending frequency and period of the LFM chirp, respectively. The zero-crossing time

$$t' = \frac{-\omega_1 + \sqrt{\omega_1^2 + 2\pi k(4n+1)}}{2k} \tag{6}$$

specifies the position of pulses along the time scale.

The in-phase reference chirped pulse (R_0) is set up through the convolution ($\otimes$) of the intensity Gaussian with a delayed Dirac delta impulse time series

$$R_0 = \left\{ \sum_{n=0}^{p} \delta \left[t - \left(\frac{-\omega_1 + \sqrt{\omega_1^2 + 2\pi k(4n+1)}}{2k} \right) \right] \right\} \otimes I_0 e^{-\frac{1}{2}\left(\frac{t}{\xi}\right)^2} \tag{7}$$

Here, p is the number of pulses to be generated. Similarly, the quadrature reference chirp (R_{90}) is synthesized from a sine LFM chirp:

DOI: 10.1038/NPHOTON.2014.111

$$R_{90}=\left\{\sum_{n=0}^{p}\delta\left[t-\left(\frac{-\omega_1+\sqrt{\omega_1^{\,2}+8n\pi k}}{2k}\right)\right]\right\}\otimes I_0 e^{-\frac{1}{2}\left(\frac{t}{\xi}\right)^2} \tag{8}$$

By convolving the thermal transient at the sample surface, equation (3), with the delayed in-phase delta impulse series, the resulting chirped-transient surface temperature, $T_{CS}(t,L)$, can be obtained:

$$\begin{aligned}T_{CS}(t,L)=&\left\{\sum_{n=0}^{p}\delta\left[t-\left(\frac{-\omega_1+\sqrt{\omega_1^{\,2}+2\pi k(4n+1)}}{2k}\right)\right]\right\}\\&\otimes\frac{[1-R]I(t)\mu_a\gamma\eta\alpha}{4K}e^{t/\tau_t}\left[erfc\left(\sqrt{t/\tau_t}\right)-erfc\left(\frac{L}{2\sqrt{\alpha t}}+\sqrt{t/\tau_t}\right)\right]\end{aligned} \tag{9}$$

The in-phase/quadrature output of the chirped-pulse photothermal radar ($Rad_{0/90}$) is calculated through the excitation-response cross-correlation as

$$Rad_{0/90}=R_{0/90}*T_{CS}(t,L) \tag{10}$$

The radar amplitude (A_{Rad}) and phase (φ_{Rad}) can be calculated from

$$A_{Rad}=\sqrt{Rad_0^{\,2}+Rad_{90}^{\,2}} \tag{11a}$$

$$\phi_{Rad}=\tan^{-1}\left(Rad_{90}/Rad_0\right). \tag{11b}$$

B. Non-ionising Bone Tomography of Bones: Volume Tomograms of Bone-Tissue Matrix

The task is to construct, through cortical and tissue overlayers, a 3D visualisation of the photothermal features of the trabecular (cancellous) bone volume where demineralisation occurs at an early stage of osteoporosis[S1]. In the context of bone mineral density (BMD) estimation and general skeletal health screening, dual energy X-ray absorptiometry (DEXA) continues to be the gold standard. Highly detailed/resolved information is provided by its variants quantitative computed tomography (QCT) and micro-computed tomography (μCT)[S2-S4]. The limitation of X-ray methods that only structural evaluation is possible has been addressed by mixed modal approaches, which couple this with other modalities, like positron emission tomography (PET), single-photon emission computed tomography (SPECT), and magnetic resonance imaging (MRI)[S5-S8]. In these cases, detailed functional and quantitative assessment is possible for bone tissues. Despite the vast potential for skeletal diagnosis, these X-ray based ionising methods are criticised for their adverse effects on tissues and poor sensitivity especially in the case of osteoporosis diagnosis. Furthermore, X-rays are attenuated only by the mineral component of bones while the organic component remains unaccounted for. Since the true bone strength depends on both these components, X-ray BMD analysis yields an incomplete picture[S9]. Another demanding situation is the BMD monitoring of astronauts under microgravity environments, as disuse osteoporosis puts them at a higher risk of fracture on return to Earth[S10,S11]. Portable and non-ionising methods suitable for continuous/ frequent bone strength monitoring are preferred in this situation. Quantitative ultrasound (QUS) and mechanical response tissue analysis (MRTA), though non-ionising counterparts of X-ray methods for BMD estimation, are short on reliability and reproducibility[S12-S14].

DOI: 10.1038/NPHOTON.2014.111

Among various biophotonic technologies, bioluminescence and fluorescence are successful agents for tracing/imaging bone metastases, tumour growth, angiogenesis, pro-angiogenic signalling, etc[S15-S17]. These methods have been optimised for whole body functional skeletal imaging of small animals with the potential for 3D tomographic reconstruction of fluorescent sources. However, poor spatial resolution, inability for discriminating the signal from cortical and trabecular sections and the depth integrated rather than depth resolved nature are their major shortcomings. Optical coherence tomography (OCT), although it offers sub-micrometer resolution and depth resolved visualisation, has its probe range limited to <1 mm in bone[S18-S19]. Another attempt made to resolve bone structure was by using diffuse optical tomography (DOT), however, its resolution was too low to observe the trabecular network[S20]. Despite their high resolution (micrometer range) and capability for depth-resolved imaging in soft tissues[S21-S24] photoacoustic tomography (PAT) and microscopy (PAM) perform poorly with bone tissues[S25-S26] due to the multiple reflections and severe attenuation of ultrasound (US) signals within the trabecular pores where high impedance-mismatch exists, especially at higher frequencies necessary for enhanced spatial and axial resolution. Since there is a severe shortage of literature on this subject, arriving at immediate conclusions on the potential of photoacoustics (PA) for bone diagnostics is impossible. So, we made a set of investigations by rerecording the PAM that does not involve any reconstruction process, and by analysing the single-point PA and US response of a few samples. The obtained results are presented in Sect. D below.

For investigating the capabilities of TC-PCT as a bone diagnosis modality, a goat rib sample with ~1.2 mm cortical thickness was analysed. It was masked with ~0.6 mm thick chicken breast tissue wrapped over it (Supplementary Figs. 2a and b) to simulate a soft tissue overlayer, and was excited with chirp-1 waveform. The imaged area was ~4.0x3.2 mm^2,

Supplementary Fig. 2b. A mild graphite powder coating was applied to the trabecular back to ensure absorption property resemblance with living bones containing marrow (hemoglobin absorption). In fact, the 0.6 mm tissue layer is too thin to be considered as a naturally or biologically accessible bone overlayer. However, this thickness offered an optimum SNR for a low enough number of continuous trials (chirped excitations) during which the tissue dehydration was negligible. With dehydration, IR transmittance increases and coupled conductive-radiative energy transfer establishes in soft issues. This would eventually lead to TC-PCT image distortion. The top surface (imaging plane) of the chicken breast layer was exposed to laser radiation. Binarised amplitude tomograms as observed from the soft tissue surface, the trabecular back and the vertical cross-section are labeled c, d and e, respectively. Here image transparency is set to 0% to ensure improved contrast for surface features. Thickness non-uniformity as well as localised variations in the thermal-wave impedance along the tissue-bone interface can be observed in Supplementary Fig. 2e. The cortical layer is well resolved and so are the trabecular interconnections below. The resolved depth in bone is about 3.6 mm.

C. TC-PCT sectioning of cortical and trabecular regions and inspection of artificially induced bone loss

Another significant advantage of TC-PCT is the ability to image sectioned cortical and trabecular regions for slice-by-slice analysis. This is accomplished by suitably selecting the number of 2D image used for volume reconstruction. Bone demineralization monitoring efficiency, a crucial parameter in osteoporosis diagnosis research, has been examined for assessing the potential of this modality in the context of non-invasive and non-ionising medical diagnostics. A goat rib piece (~4.0x1.5x0.5 cm^3) with cortical thickness ~0.7 mm was chemically etched for 0.5 and 10 hours (Supplementary Figs. 3 A1-3), in two stages, using 0.5 M ethylenediaminetetraacetic acid

DOI: 10.1038/NPHOTON.2014.111

(EDTA) diluted with an equal volume of distilled water (50% EDTA). The EDTA solution produces a very slow and gentle decalcification and its mild solution (pH ≤ 8) has been widely used in the literature for simulating artificial osteoporosis [S27-S29]. Since the dependence of the degree of demineralization on the etching parameters such as EDTA concentration, etching time, etc., was not precisely known, this was a non-standardised demineralisation process. The bone was irradiated on the top cortical surface which was the plane of imaging ($z = 0$).

Supplementary Figs. 3 B1-3 show the TC-PCT binary volume images (4.0x3.2x2.8 mm^3) of this sample, before (B1) and, after demineralisation for 0.5 hour (B2) and 10 hours (B3), as viewed from the trabecular bottom. Here, binarised amplitude TC-PCT images are used for volume reconstruction and 50% layer transparency is maintained to see the interior. Supplementary Videos 1, 2 and 3 contain 360˚ views of the combined cortical-trabecular tomograms of the intact, 0.5- , and 10-hour demineralised ribs, respectively. Video 1 clearly shows the trabecular network resolved through the light scattering cortical layer (intact). In Video 2, when compared with Video 1, changes to the cortical and trabecular regions due to mild chemical demineralisation can be observed. Video 3 depicts changes due to trabecular collapse following prolonged demineralization. To further examine how TC-PCT tracks the cortical and trabecular changes due to this artificial osteoporosis, two ~300 μm thick layers were extracted, one from the cortical surface and the other from a depth of ~1.5 mm below it. C1-3 are the top views of the surface slice and D1-3 show the respective bottom views. The E and F series depict the top and bottom surfaces of the ~1.5 deep layer. In all cases 1, 2 and 3 denote the intact, 0.5-hour and 10-hour demineralised sample, respectively. Image transparency was set to 0% for the improved contrast of surface features. The arrows on the intact-sample images indicate prominent regions of damage noticeable even in the mild demineralisation case. Supplementary Fig. 4 is the

conventional lock-in thermography (LIT) depth-integrated image obtained for the intact rib (Supplementary Fig. 3 A1) at 0.2 Hz harmonic modulation of the same laser, the power being attenuated to ~2 W (peak). The field of imaging remained the same as that of TC-PCT. It was impossible to monitor any demineralisation changes with LIT, even at an advanced stage (10 h). The finding of excellent TC-PCT sensitivity to cortical bone density changes, despite the fact that osteoporotic density changes are more pronounced in the trabecular network[S30], is very promising for in-vivo early bone osteoporosis diagnostic imaging applications of this technology as there is no absolute need for light penetration into the trabecular region. This fact works well with the relatively shallow sub-surface penetration ability of thermal waves and points to future clinical use of this technology for the non-invasive imaging and diagnostics of near-surface human bones like wrist, calcaneus and tibia.

D. Comparison of TC-PCT with other nonionising, depth-resolved modalities for bone diagnostics

In terms of depth-resolved visualization and non-ionising advantages, PA and US imaging, as well as OCT are the modalities most comparable with bone TC-PCT. We have generated experimental results for PA and US and we are referring to the existing reports for OCT capabilities[S31-S33]. Our single point PA probe consists of a 2-mm diameter collimated excitation laser beam (808 nm) with a 3-MHz transducer (low frequency for deep penetration at a loss of spatial resolution). The US probe used a pair of 3-MHz transducers as transmitter and receiver. The demineralisation agent was made by diluting 20 ml of EDTA solution with 80 ml of distilled water. A goat rib sample, ~15x10x4 mm^3, (Supplementary Fig. 5a) was analysed intact and after 22- and 44-hour demineralisation with both methods. The PA and US signal envelopes are

DOI: 10.1038/NPHOTON.2014.111

shown as a function of delay-time in Supplementary Figs. 5b and 5c, respectively. This delay was estimated through the signal-reference cross-correlation. The sample was examined at 7 points along a line. The results show that the PA signal from the surface (cortical) layer decreases with demineralisation, whereas the US signal is insensitive to changes in this layer. The US signal from the underlying trabecular region decreases with demineralisation while the trend of PA signal is unpredictable: sometimes it decreases, other times it increases. Although PA sensitivity to cortical changes could only be measured after 5 hours of demineralisation in 50% EDTA, the trend is similar to that of TC-PCT which can resolve such changes after 0.5-hour demineralisation.

In another experiment, PA and US backscattering signals from a trabecular bone block of human calcaneus were analysed. The human bone lost its marrow and had reduced lipid elements following the cleaning procedure, however the minerals were left intact. The size of the bone was 15.7x15.7x35.0 mm^3. On one side of the bone some holes (1 mm diameter) were drilled, while the other side remained intact. The thickness of bone layer above these holes was different. PA and US spectra were averaged for measurements at 6 points on the intact regions and 6 points over the holes. In both cases the response was found to be insensitive to the changes in the bone layer thickness above 3 mm, thereby limiting their depth range in bones to $\leq$ 3 mm at 3 MHz.

PAM was recorded at 20 MHz for a rib sample of thin (~0.5 mm) cortical layer, (Supplementary Fig. 6) with 690-nm, 8-ns optical excitation with 10 Hz repetition frequency. Exposure energy density was ~0.03 mJ/mm^2 per pulse. Both bone-water interface and sub-cortical structure appear in the image. However, the latter is assumed to be a composite picture of both PA signal and backscattered US contribution from the trabeculae. At 50 MHz, with all other settings the same, neither the sub-cortical pattern nor the cortical-water interface was

resolved clearly. To understand the true mechanism responsible for the trabecular contrast, further research is needed in this direction.

E. Burn Assessment Technologies

Among various clinically effective methods in current use, infrared thermography has gained considerable acceptance for its non-contacting nature. It estimates the wound temperature assuming deeper burns have lower blood supply, however, the impossibility of depth-resolved visualisation and the influence of ambient temperature variations on burn severity assessment are the major limitations of this approach. Fluorescence video-angiography with intravenous indocyanine injection offers excellent agreement with histological validations although safety concerns exist for use of this dye with pregnant, paediatric and lactating patients. Near-infrared spectroscopic imaging, while capable of differentiating between oxy- and deoxy- haemoglobin, has been criticized for its accuracy deterioration by physiological effects other than thrombosis. Similar to thermography, depth-resolved wound visualisation is not possible with this method. Despite the advantage of quantifying the distribution of red blood cells, Laser Speckle Imaging (LSI) shares the shortcoming of depth-integrated visualisation with other methods, thereby heavily compromising axial resolution. Among various non-invasive methods, Laser Doppler Imaging (LDI) enjoys the highest acceptance for clinical use with ~95% agreement with histological results. It is fast and accurate for diagnosing both large and small wounds in stable patients. However, its disadvantages are many: results are affected by angle of inspection, ambient temperature, wound-to-detector distance, patient blood pressure variations, etc. Furthermore, depth-resolved assessment is not possible with this modality. Reflectance-Mode Confocal Microscopy (RMCM) and OCT facilitate depth-resolved burn assessment, however,

DOI: 10.1038/NPHOTON.2014.111

within a very limited range, <1 mm. Another potential modality is photoacoustic microscopy, which depicts the 3D distribution of optical absorption and acoustic properties of the burnt-tissue. The need of water for high-frequency ultrasound coupling and point-by-point raster scanning that demands the patient to be static are its shortcomings[S26, S34, S35].

Supplementary References

S1. Bartl, R. & Frisch, B. *Osteoporosis: Diagnosis, Prevention, Therapy* (Springer-Verlag, Berlin, 2009).

S2. Bonnick, S.L. *Bone Densitometry in Clinical Practice: Application and Interpretation* (Humana Press, New York, 2010).

S3. Blake, G.M. & Fogelman, I. Role of dual-energy X-ray absorptiometry in the diagnosis and treatment of osteoporosis. *J. Clin. Densitom*. **10**, 102-110 (2007).

S4. Ritman, E.L. Current status of developments and applications of micro-CT. *Annu. Rev. Biomed Eng*. **13**, 531–552 (2011).

S5. Li, Z.C., Jiang, S.D., Yan, J., Jiang, L.S. & Dai, L.Y. Small-animal PET/CT assessment of bone microdamage in ovariectomized rats. *J. Nucl. Med*. **52**, 769–775 (2011).

S6. Linke, R., Kuwert, T., Uder, M., Forst, R. & Wuest, W. Skeletal SPECT/CT of the peripheral extremities. *Am. J. Roentgenol*. **194,** W329–W335 (2010).

S7. Genant, H.K., Engelke, K. & Prevrhal, S. Advanced CT bone imaging in osteoporosis. *Rheumatology*. **47,** iv9–iv16 (2008).

S8. Kaijzel, E.L., Snoeks, T.J.A., Buijs, J.T., van der Pluijm, G. & Lowik, C.W.G.M. Multimodal imaging and treatment of bone metastasis. *Clin. Exp. Metastasis,* **26**, 371–379 (2009).

S9. Draper, E.R.C. *et al.* Novel assessment of bone using time-resolved transcutaneous Raman spectroscopy. *J. Bone Miner Res*. **20**, 1968–1972 (2005).

S10. Vico, L. *et al*. Effects of long-term microgravity exposure on cancellous and cortical weight-bearing bones of cosmonauts. *Lancet*. **355**, 1607-1611 (2000).

S11. NASA HRP-47060. *Evidence Book: Risk of Accelerated Osteoporosis*. Lyndon B Johnson Space Center, Texas, USA:2008.

S12. Nayak, S. *et al.* Meta-analysis: Accuracy of ultrasound for identifying patients with osteoporosis. *Ann. Intern. Med*. **144**, 832-841(2006).

S13. Djokoto, C., Tomlinson, G., Waldman, S., Grynpas, M. & Cheung, A.M. Relationship among MRTA, DXA, and QUS. *J. Clin. Densitom*. **7**, 448–456 (2004).

S14. Roberts, S.G. *et al.* Noninvasive determination of bone mechanical properties using vibration response: a refined model and validation in vivo. *J. Biomechanics.* **29**, 91-98 (1996).

S15. Snoeks, T.J.A., Khmelinskii, A., Lelieveldt, B.P.F., Kaijzel, E.L. & Lowik, C.W.G.M. Optical advances in skeletal imaging applied to bone metastases. *Bone*. **48**, 106-114 (2011).

S16. Kozloff, K.M., Weissleder, R. & Mahmood, U.J. Noninvasive optical detection of bone mineral. *J. Bone Miner. Res.* **22**, 1208–1216 (2007).

S17. Vatsa, A. *et al.* Bio imaging of intracellular NO production in single bone cells after mechanical stimulation. *J. Bone Miner. Res.* **21**, 1722–1728 (2006).

S18. Kasseck, C. *et al.* Comparison of optical coherence tomography, microcomputed tomography, and histology at a three-dimensionally imaged trabecular bone sample. *J. Biomed. Opt*. **15**, 046019 (2010).

DOI: 10.1038/NPHOTON.2014.111

S19. Beaudette, K. *et al.* Optical coherence tomography for the identification of musculoskeletal structures of the spine: a pilot study. *Biomed. Opt. Express*. **3**, 533-542 (2012).

S20. Xu, Y., Iftimia, N., Jiang, H., Key, L.L. & Bolster, M.B. Three-dimensional diffuse optical tomography of bones and joints. *J. Biomed. Opt*. **7**, 88-92 (2002).

S21. Xu, M. & Wang, L.V. Photoacoustic imaging in biomedicine. *Rev. Sci. Instrum.* **77**, 041101 (2006).

S22. Yang, J.M. *et al.* Simultaneous functional photoacoustic and ultrasonic endoscopy of internal organs in vivo. *Nat. Med*. **18**, 1297-1302 (2012).

S23. Silverman, R.H. *et al.* High-resolution photoacoustic imaging of ocular tissues. *Ultrasound Med. Biol.* **36**, 733-42 (2010).

S24. Wang, L.V. Multiscale photoacoustic microscopy and computed tomography *Nat. Photonics* **3**, 503-509 (2009).

S25. Nie, L. *et al.* Photoacoustic tomography through a whole adult human skull with a photon recycler. *J. Biomed. Opt*. **17**, 110506 (2012).

S36. Wang, X. *et al*. Imaging of joints with laser-based photoacoustic tomography: An animal study. *Med. Phys*. **33**, 2691-2697 (2006).

S27. Callis, G. & Sterchi, D. Decalcification of bone: Literature review and practical study of various decalcifying agents, methods, and their effect on bone histology. *J. Histotechnology* **21**, 49-58 (1998).

S28. Ehrlicha, H., Koutsoukos, P.G., Demadis, K.D. & Pokrovsky, O.S. Principles of demineralization: Modern strategies for the isolation of organic frameworks, Part II. Decalcification. *Micron* **40**, 169-193 (2009).

S29. Hoffmeister, B.K., Whitten, S.A., Kaste, S.C. & Rho, J.Y. Effect of collagen and mineral content on the high-frequency ultrasonic properties of human cancellous bone. *Osteoporos Int.* **13**, 26-32 (2002).

S30. Langton, C. Osteoporosis: case of skeletal biocorrosion. *Corrosion Eng. Sci. Technol*. **42**, 339-343 (2007).

S31. Drexler, W. Ultrahigh-resolution optical coherence tomography. *J. Biomed. Opt.* **9**, 47–74 (2004).

S32. Tsai, T. *et al.* Ultrahigh speed endoscopic optical coherence tomography using micromotor imaging catheter and VCSEL technology. *Biomed. Opt. Express* **4**, 1119-1132 (2013).

S33. Jacobs, J.W. & Matcher, S.J. Polarization sensitive optical coherence tomography in equine bone. *Proc. SPIE* ***7166***, Optics in Bone Biology and Diagnostics, 716608 (2009).

S34. Sato, S. *et al.* Photoacoustic diagnosis of burns in rats. J. Trauma **59**, 1450-1456 (2005).

S35. Zhang, H.F., Maslov, K., Stoica, G. & Wang, L.V. Imaging acute thermal burns by photoacoustic microscopy. *J Biomed. Opt.* **11**, 054033 (2006).

DOI: 10.1038/NPHOTON.2014.111

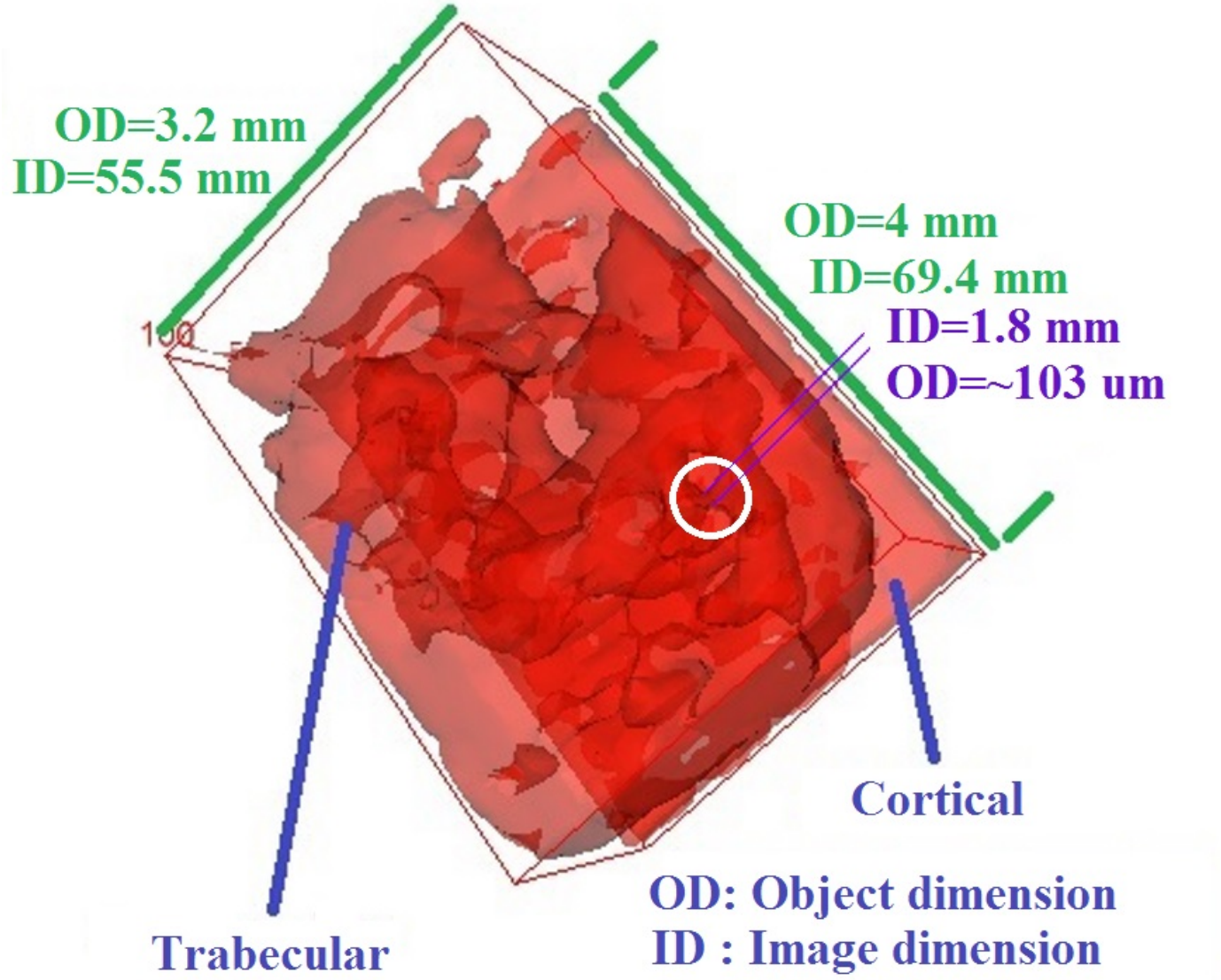

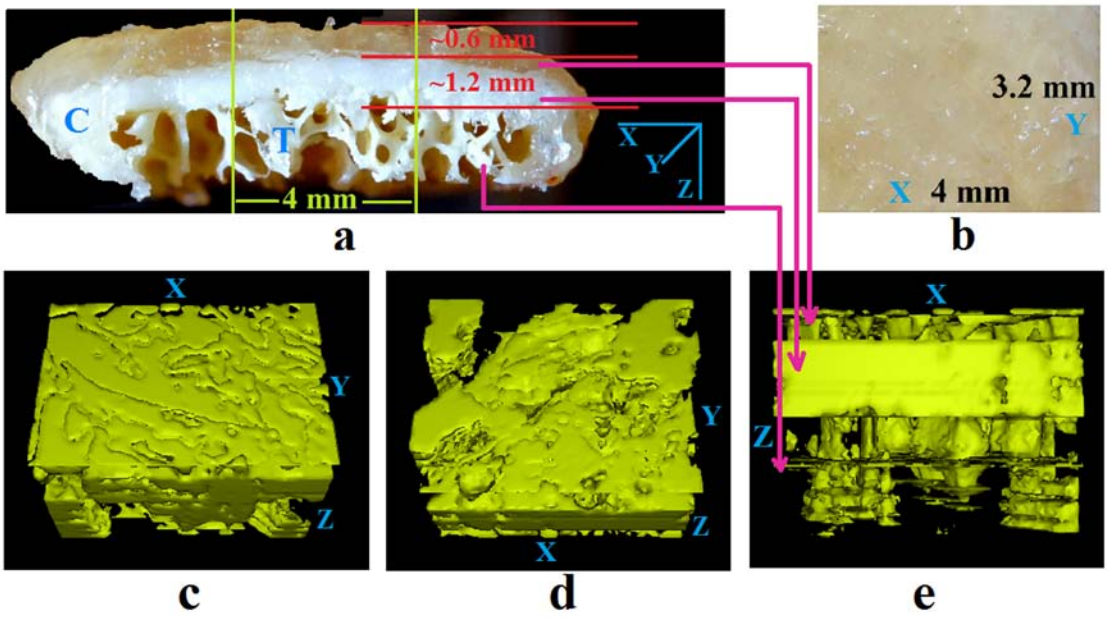

DOI: 10.1038/NPHOTON.2014.111

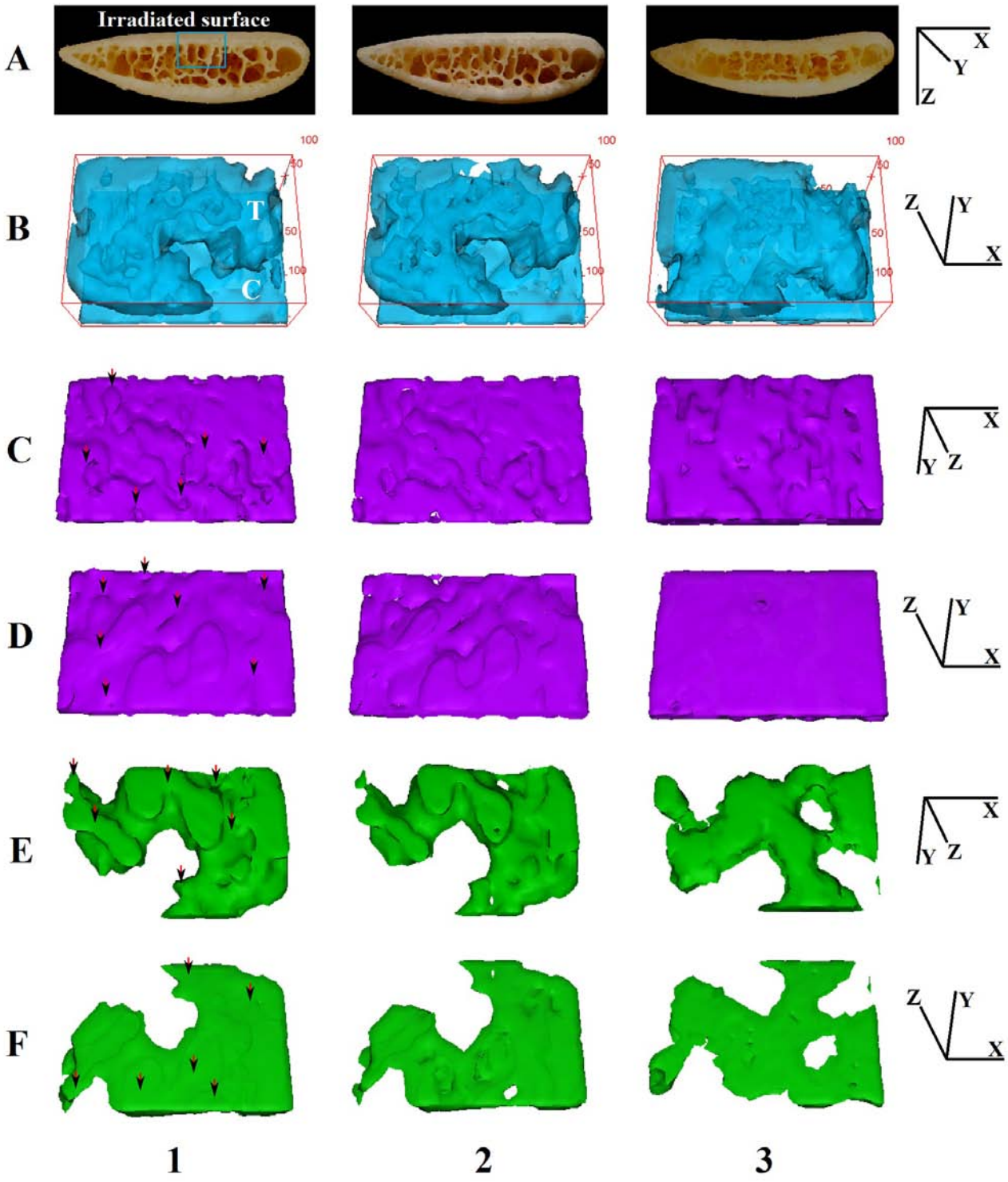

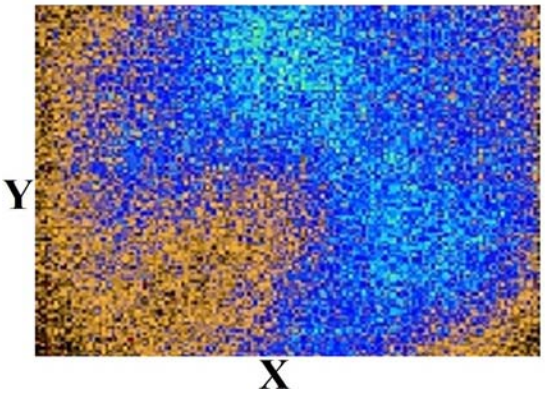

DOI: 10.1038/NPHOTON.2014.111

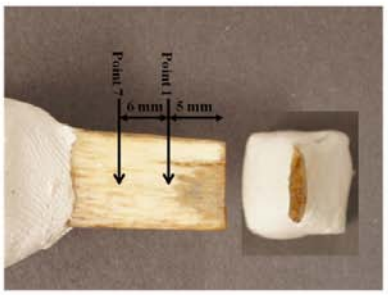

(a)

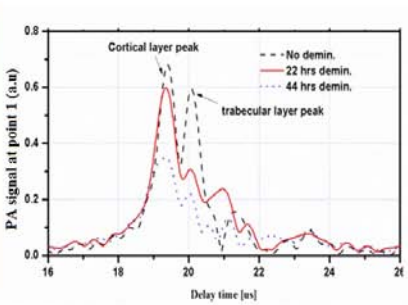

(b)

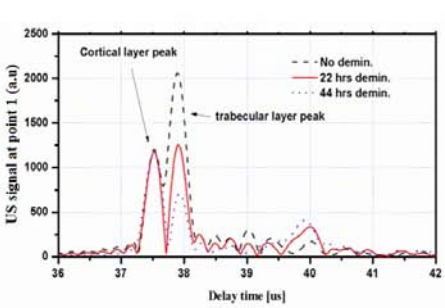

(c)